Nanoscale

Accepted Manuscript

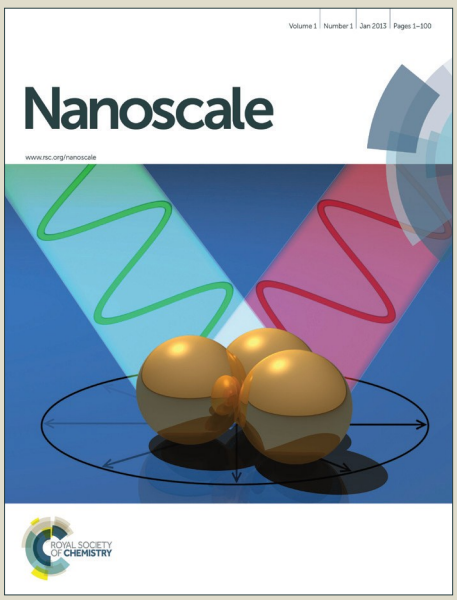

ROYAL SOCIETY OF CHEMISTRY

www.rsc.org/nanoscale

Journal Name

ARTICLE

Design of multi-shell Fe_2O_3@MnO_x@CNTs for the selective catalytic reduction of NO with NH_3: improvement of catalytic activity and SO_2 tolerance

Received 00th January 20xx,
Accepted 00th January 20xx

DOI: 10.1039/x0xx00000x

www.rsc.org/

Sixiang Cai,[a] Hang Hu,[b] Hongrui Li,[b] Liyi Shi [ab] and Dengsong Zhang[ab]*

The manganese based catalysts are highly active in the NH_3-SCR reaction for the NO_x removal. Unfortunately, the manganese oxides can be easily deactivated by the sulfur dioxide in the flow gas, which has become the main obstacle for its practical applications. To address this problem, we presented a green and facile method for the synthesis of multi-shell Fe_2O_3@MnO_x@CNTs. The morphology and structure properties of the catalysts were systematically investigated. The results revealed that the MnO_x@CNTs core-shell structure was formed during the chemical bath deposition, while the outermost MnO_x species were transformed to Fe_2O_3 after the galvanic replacement reaction. The formation of the multi-shell structure induced the enhancement of the active oxygen species, reducible species as well as adsorption of the reactants, which brought about excellent de-NO_x performance. Moreover, the Fe_2O_3 shell could effectively suppress the formation of the surface sulfate species, leading to the desirable SO_2 resistance to the multi-shell catalyst. Hence, the synthetic protocol could provide guiding for the preparation and elevation of manganese based catalysts.

1. Introduction

Currently, the selective catalytic reduction (SCR) is one of the most promising technologies for the removal of the harmful nitrogen oxides (NO_x) resulting from the fossil fuel combustion.[1-4] For decades, the vanadium-based deNO_x catalysts have been adopted to industrial applications.[5-7] However, this catalyst system is inevitably hampered by the poor low temperature catalytic activity and the toxicity for vanadium pentoxide.[7-9] In this regard, great efforts have been devoted to develop vanadium-free SCR catalysts.

Manganese oxides, which is famous for its inherent environmental benign character and superior catalytic activity in the deNO_x reaction, has been considered as a promising candidate as the de-NOx catalyst.[10-13] To further enhance the catalytic activity in the low temperature range, various supported manganese catalysts have been investigated ,which demonstrate excellent de-NO_x behavior below 300 ^oC.[14-17] Recently, we have reported a Mn@CNTs based SCR catalyst *in-situ* prepared via a chemical bath deposition route. The synthesis pathway and the CNTs carrier bring large surface area and Mn species with high valence state, leading to the favorable NH_3-SCR activity in the low temperature range.[19-21] Nonetheless, like other manganese based catalysts, the Mn@CNTs catalysts can be easily deactivated by SO_2 in the flow gas,[22,23] which become the main obstacle for its practical applications.

Due to the environmental-friendly, low cost and good sulfur tolerance, the ferric oxides have been studied to catalyze the NH_3-SCR reaction in the past few years.[24-31] For instance, Qu et al. used a simple ethanol-assisted impregnation method to prepare the Fe_2O_3/CNTs catalysts and showed over 90% NO conversion and selectivity between 200-325 ^oC. [25]What's more, the absence of SO_2 gas could even strengthen the surface acid sites of the catalysts, thereafter promote the SCR activity. Li et al. investigated several Fe based catalysts and found the sulfated Fe-Ti spinel catalysts demonstrated outstanding SCR activity, N_2 selectivity as well as the H_2O+SO_2 tolerance within 300-450 ^oC.[26] However, the catalytic activity of the Fe based catalysts at low temperature still remains unsatisfactory.

To overcome the intrinsic shortcoming of the Fe and Mn based catalysts, it is of great interest to develop new de-NO_x catalyst combining the unique characteristics of ferric oxides and manganese oxides. Herein, we designed a facile and green way for the synthesis of a novel de-NO_x catalyst with Fe_2O_3@MnO_2@CNTs multi-shell structure. As demonstrated in Fig.1, the MnO_2 nanoflakes were firstly deposited on the surface of CNTs to form a core-shell structure *via* a chemical bath deposition route. The architecture could provide a high level of Mn^{4+} concentration and a large specific surface area, which could be conducive to the following transformation and

[a] School of Material Science and Engineering, Shanghai University, Shanghai 200072, China. E-mail: dszhang@shu.edu.cn; Fax: +86 21 66136079
[b] Research Center of Nano Science and Technology, Shanghai University, Shanghai 200444, China.

Electronic Supplementary Information (ESI) available: Experimental details and catalytic performance of the Fe-Mn@CNTs IM, TEM images of Fe@Mn CNTs, stability and H_2O resistance studies of the catalysts.

the de-NO_x process.[21, 32] Subsequently, the Fe^{2+} containing

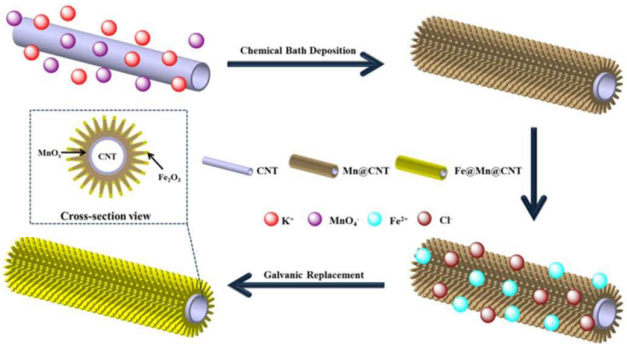

Fig.1 Schematic representation of the synthesis route of Fe_2O_3@MnO_x@CNTs multi-shell catalysts.

solution was added into the suspension of MnO_2 decorated CNTs to trigger the galvanic replacement reaction. The galvanic exchange reaction rely on the different reduction potentials (MnO_2/Mn^{3+}= 0.91V, Fe^{3+}/Fe^{2+}=0.77V) and could complete the uniformly transformation from MnO_2 to Fe_2O_3 without damaging the initial structure of the catalyst.[33] The *in-situ* formation of the Fe_2O_3 sheaths could bring about a strong interaction between Fe and Mn species and effectively suppress the poisoning effect of SO_2. In our expectation, the catalyst with varied chemical composition would combine the advantages of the high sulfur resistance and N_2 selectivity of the Fe_2O_3 shell, the excellent low temperature de-NO_x performance of the MnO_2 interlayer and the great gas adsorption capacity of the CNTs core. Finally, the morphology, structure properties as well as the catalytic performance of catalysts were also systematically investigated.

2. Experimental Section

Catalysts preparation

All reagents, supplied by Sinopharm Chemical Reagent Co. Ltd (China), were of analytical grade and used without further purification. The multi-walled CNTs were purchased from Qinghuangdao Tai Chi Ring Nano Product Co. Ltd (China). Before use, the CNTs were refluxed in 80% HNO_3 aqueous solution at 140 °C for 6 h, washed with deionized water to remove residual HCl, and then dried at 80 °C overnight.

The MnO_2 coated CNTs were prepared by a chemical bath deposition route reported in our previous work (denoted as Mn@CNTs) with some modifications.[21] Typically, 0.36 g of the $KMnO_4$ was dissolved in 200 ml of deionized water and then 0.2 g of the acid-treated CNTs was well dispersed in the violet solution under ultrasonic vibration. Subsequently, 15 ml of acetic acid was added into the suspension and the mixture was heated to 70 °C for 1 h under stirring. The product was collected by filtration, washed with distilled water and dried overnight at 80 °C.

The further transformation from MnO_2 to Fe_2O_3 was completed *via* the following reaction path way. Firstly, 0.5 g of the Mn@CNTs was dispersed in 250 ml of deionized water under the ultrasonic vibration for 0.5 h. Then, the suspension was heated to 80 °C under continuous stirring. Subsequently, the aqueous solution containing appropriate amounts of $FeCl_2{\cdot}4H_2O$ were slowly added into the suspension to trigger the galvanic replacement reaction. After 1 h of stirring, the products were filtered and washed completely with distilled water. Finally, the nanocomposites were dried overnight at 80 °C and denoted as Fe@Mn@CNTs and Fe@CNTs (the completely transformed sample).

Catalyst characterization

The Powder X-ray diffraction (XRD) was measured by a Rigaku D/MAX-2200 X-ray diffractometer with Cu-Ka (40 kV, 40 mA) radiation and a secondary beam graphite monochromator. The transmission electron microscope (TEM) observation was carried out on a JEOL JEM-200CX system. Energy dispersive X-ray (EDX) analysis and the elemental mapping were conducted using an Inca Energy 200 TEM system from Oxford Instruments. The X-ray photoelectron spectroscopy (XPS) measurements were conducted on a RBD upgraded PHI-5000C ESCA system with a hemispherical energy analyzer using an Mg-Ka (1253.6 eV) anode and a dual X-ray source. The binding energies referring to O, Fe and Mn were corrected according to contaminant carbon (C 1s = 284.6 eV) and the peak fitting was performed by using AugerScan (version 3.21) software. Temperature-programmed reduction by hydrogen (H_2-TPR) was carried out on a Tianjin XQ TP 5080 auto-adsorption apparatus. Before the reduction process, 40 mg of each catalyst was outgassed at 300 °C for 30 min and then cooled down to room temperature. Afterwards, the inlet gas was switched to 10 % H_2/Ar and the reaction temperature was heated to 700 °C with a heating ramp of 10 °C·min^{-1} and the H_2 consumption data was recorded by a thermal conductivity detector (TCD). Temperature-programmed desorption (TPD) experiments of NH_3, NO+O_2 and SO_2+O_2 were performed on the same apparatus. Prior to TPD, 200 mg of catalysts were outgassed under 300 °C for 0.5 h and then cooled to 100 °C (under Ar protection). For NH_3-TPD, the catalysts were saturated with high-purity anhydrous ammonia at 100 °C for 90 min and then the physisorbed ammonium was removed at the same temperature by 1 h Ar flow flushing. Finally, the NH_3-TPD process was carried out at a ramping rate of 10 °C·min^{-1} with the protection of Ar flow. For NO+O_2-TPD and SO_2+O_2-TPD, the adsorption was performed by passing a mixed gas containing 500 ppm NO + 5% O_2 or 500 ppm SO_2+ 5% O_2 with He as the balance at room temperature for 1h and subsequently flushed for another 1h. Finally, the operation was carried out at a heating rate of 10 °C min^{-1}. The TCD was used as monitor to calculate the amount of desorbed gas in all TPD experiments. Thermo gravimetric analysis (TGA, NETZSCH STA 449 F1) was performed to realize the thermal decomposition characteristics of fresh catalysts and the spent catalysts after the SO_2 tolerance test. The temperature was raised from room temperature to 700 °C with a ramping rate of 10 °C/min.

Catalyst performance tests

The NH_3-SCR activity tests were performed in a fixed-bed quartz reactor (8 mm of internal diameter) operating with steady state flow. Prior to the SCR test, 0.2 g of catalysts with 40-60 mesh and 50 mg quartz wool (to avoid the axial

diffusion) was placed into the reactor. The composition of the reactant feed gas was listed as follow: [NO] = [NH_3] = 550 ppm, [O_2] = 5 vol. %, [SO_2] = 100 ppm (when used), [H_2O] = 10 vol. % (when used), N_2 as balance gas, the gas hourly space velocity (GHSV) was set to 20,000 h^{-1}. The catalytic activity in the SCR reaction was recorded until the reaction reached a steady state. The concentrations of NO in the feed gases and the effluent streams were analyzed continuously by a KM9106 flue gas analyzer. The NO conversion was calculated according to the following expression and each catalyst was tested for 3 times to calculate the average quantitative value of the NO conversion:

$$\text{NO conversion } (\%) = \frac{[NO]_{in}-[NO]_{out}-[NO_2]_{out}}{[NO]_{in}} \times 100\%$$

3. Results and discussion

Characteristics of the catalysts

The XRD patterns of the catalysts are demonstrated in Fig.2. For Mn@CNTs, the diffraction peaks located at 26°, 43° and 54° can be assigned to the (002), (101) and (004) reflections of the CNTs.[34] Meanwhile, the peaks centered at 12°, 37° and 66° are the characteristic diffraction of the δ-MnO_2 (JCPDS 42-1317), which suggest the deposition of Mn oxides on the CNTs surface.[21] It is worth noticing that the characteristic peaks of δ-MnO_2 become weaker and broader after the galvanic reaction, indicating the decreased crystal size, crystallinity degree as well as the consumption of the Mn species during the reaction process. Meanwhile, no additional peak derived from Fe species can be detected in the diffraction pattern of Fe@Mn@CNTs. The result illustrated the amorphous characteristic and the satisfactory dispersion of the Fe species on the exterior of the catalysts. The characteristic peaks of the Mn species vanished, while the peaks of α-Fe_2O_3 phase (JPCDS 33-0664) and γ-Fe_2O_3 (JPCDS 13-0458) appeared in the XRD patterns of the Fe@CNTs,[31] indicating the complete transformation on the catalyst surface. Besides, the three catalysts demonstrate poor signal to noise, which is always related to the low crystallinity or low loading rate of or low loading amounts of the catalysts. In order to reveal the loading amounts of the active species on the CNTs supports, the TGA

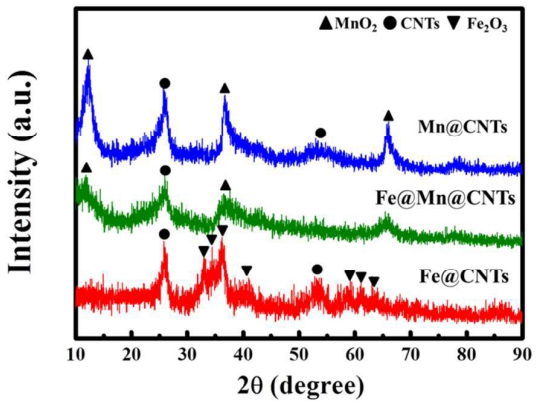

Fig.2 XRD patterns of the catalysts.

analysis has been conducted and the weight percentage of the metal oxide species were 61.3%, 59.0% and 59.2% for amounts of the catalysts. In order to reveal the loading amounts of the active species on the CNTs supports, the TGA analysis has been conducted and the weight percentage of Mn@CNTs, Fe@Mn@CNTs and Fe@CNTs (Table S1, ESI), respectively. Thus, it can be confirmed that the weak signal of the catalysts is mainly originated from the amorphous structure of the surface metal oxide species.

The TEM observation was conducted to investigate the micro-morphologies of the catalysts. As elucidated in Fig.3a, through the chemical bath reaction, the outer surface of the CNTs was covered by various small MnO_x nanoflakes, constructing a core-shell structure. In the case of the Fe@Mn@CNTs (Fig.3b), the core-shell structure was well inherited after the partial galvanic displacement from MnO_x to Fe_2O_3. However, for the Fe@CNTs, the flake like metal oxides located on the CNTs were detached and aggregated around the CNTs (Fig.S1, ESI). As well documented in the literature, this structure-breakup phenomenon usually occurred with the complete sacrifice of the template.[35] Thus, the observation could indicate to the perfect transformation from manganese oxides to ferric oxides. Meanwhile, the HR-TEM image (Fig.3c) showed that the MnO_x nanoflake was anchored on the CNTs surface with the width of 5 nm. In addition, some of the lattice images of different form carbon did exist in the HR-TEM observation but most of them were too indistinct to identify, which indicates most of MnO_x and Fe_2O_3 species were in the amorphous or quasi-crystal form. To reveal the spatial distribution of the corresponding elements in the Fe@Mn@CNTs, the elemental mapping technique was performed and the results were presented in Fig. 3d-h. Interestingly, the Fe species were mainly located on the outer layer of the nanocomposite, while the signal of Mn occurred in the middle layer and the C signal can only be observed in the interior of the catalyst. The result confirmed the uniformly substitution from MnO_x to Fe_2O_3 in the outer surface, which agrees well with the previous reports.[33,36] The Fe_2O_3 species could serve as an effective barrier to reduce the formation of manganese sulfate, which could lead to enhanced SO_2-resistance performance to the Fe@Mn@CNTs catalyst.

The N_2 sorption was conducted to determine the porous structure and the specific surface area of the catalysts. From

the nitrogen adsorption–desorption isotherms demonstrated in Fig.4, all of the catalysts exhibit type IV sorption isotherms and type H_3 hysteresis loops, which reflect the mesoporous structure of the catalysts.[34, 37] The surface areas and pore volumes of Mn@CNTs ,Fe@Mn@CNTs and Fe@CNTs are listed in Table S1. As shown clearly, all of the catalysts show similar surface area around 170 m^2/g. The high surface area is mainly induced by the CNTs support, which could provide ideal adsorptive and reactive centers for the reagent gases.[38] The pore size distribution was calculated using BJH model. As shown in Fig.4 (Inset), both of the Fe@Mn@CNTs and Mn@CNTs catalysts exhibit similar pore distribution. The pore size around 2 nm results from the internal cavity of CNTs, [32] while the pore range of 10-20 nm are contributed by the staggered arrangement of the manganese oxides on the CNTs surface.[18] Those features reveal that the formation of the

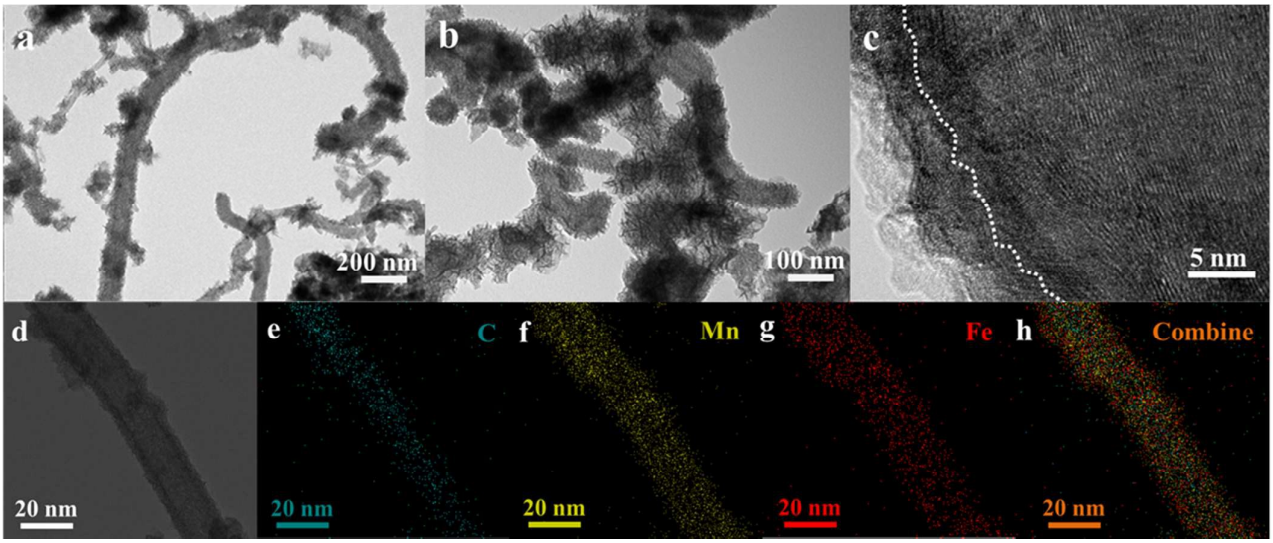

Fig.3 TEM images of a) Mn@CNTs, b) Fe@Mn@CNTs, c) HR-TEM image of the Fe@Mn@CNTs, d) HAADF-STEM image of the Fe@Mn@CNTs, and e-h) Elemental mapping images of Fe@Mn@CNTs.

multi-shelled structure without damaging the initial structure of the Mn@CNTs, which agree well with the TEM observation. Nonetheless, in the case of Fe@CNTs, the pore distribution of the Fe@CNTs is distinctly changed. The detachment and agglomeration of the flake like structures (Fig.S1, ESI) could be the main reason for the alteration of the pore structure.

The XPS analysis is conducted to reveal the near surface composition as well as the valance state of the elements. The mole fractions of the elements are summarized in Table 1. As for the Mn@Fe@CNTs catalyst, the mole ratio of Fe/Mn (1.41) is much higher than the designed value (0.2), suggesting that the Fe species are mainly located on the outer-surface of the nano-flaky structure. This result is in good conformity with the EDS-mapping observation. It is worth noticing that the Mn signal vanishes in the Fe@CNTs, indicating all of the Mn species are replaced by the Fe species, which agrees well with the XRD results.

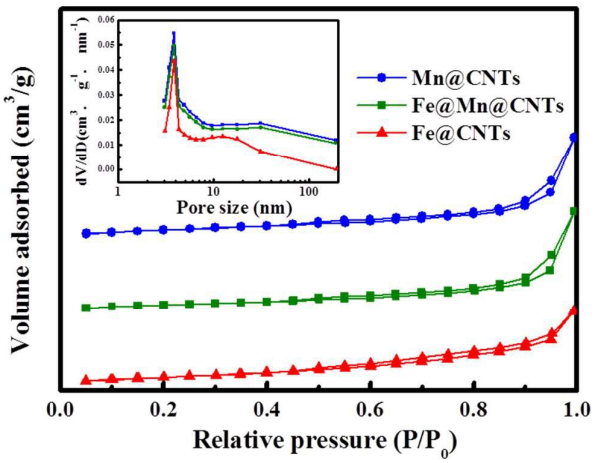

Fig.4 N_2-desorption results of the catalysts; (inset) Pore distribution of the catalysts.

As shown in Fig.5a , the O 1s XPS spectra are fitted into two peaks corresponding to the lattice oxygen (O_β, centered at 529.6 eV) and the surface-absorbed oxygen from the oxide defects or hydroxyl groups (O_α, centered at 531.8 eV), respectively.[39] According to the XPS results, the amount of O_α species on the Fe@Mn@CNTs (66.2%) is higher than the Mn@CNTs (60.1%) catalysts, which could be related to the formation of oxide defects and hydroxyl groups during the galvanic replacement reaction. However, when the manganese oxides were completely transformed to ferric oxides, the O_α species for the Fe@CNTs were decreased to 56.6%. On one hand, the abundant O_α species could promote NO oxidation ability and then facilitates the "Fast SCR" process.[40,41] On the other hand, the enriched surface hydroxyl-like groups could act as Brønsted sites to absorb NH_3 and form NH^{4+} species.[42] Hence, the moderate galvanic displacement is crucial in preparing highly effective NH_3-SCR catalysts.

By peak-fitting deconvolutions, the XPS spectra of Mn $2p_{3/2}$ are split into three peaks assigned to Mn^{2+} (640.5 eV), Mn^{3+} (642.2 eV) and Mn^{4+} (644.3 eV), respectively. As demonstrated in Table 1, the concentration ratios of Mn^{4+} declined after the galvanic replacement reaction. However, the Mn^{2+} and Mn^{3+} ratio were both increased. It has been demonstrated that the Mn ions with high valance state (Mn^{4+} and Mn^{3+}) could react with the Fe^{2+} ion in the galvanic replacement reaction and

Journal Name

ARTICLE

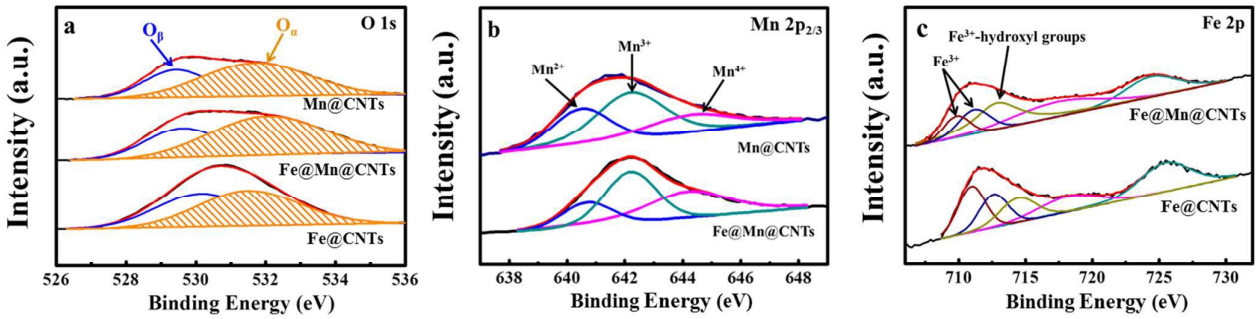

Fig.5 XPS results for a) O 1s, b) Mn $2p_{3/2}$ spectra and c) Fe 2p spectra of the catalysts.

derived to the formation of the Fe_2O_3 shell. [33] Therefore, the decrease of the Mn^{4+} as well as the rise of Mn^{2+} and Mn^{3+} is generated by the transformation during the galvanic replacement reaction. Due to the high oxidation ability of Mn^{4+} species, a high Mn^{4+} concentration is favorable for the low temperature NH_3-SCR performance. In that case, the decline of Mn^{4+} could result in the loss of low temperature catalytic activity of Fe@Mn@CNTs catalyst. Nonetheless, the Mn^{4+} species are related to the non-selective oxidation of NH_3. Therefore, the catalytic selectivity should be enhanced during the NH_3-SCR reaction. Besides, the increased Mn^{3+} ratio could make contribute to the enrichment of the redox cycle ($Mn^{3+} \leftrightarrow Mn^{4+} + e$) of the Fe@Mn@CNTs catalyst.[12]

Both of the Fe@Mn@CNTs and Fe@CNTs (Fig. 5c) exhibit two distinct peaks located at 711.3 and 724.7 eV ascribed to Fe $2p_{3/2}$ and Fe $2p_{1/2}$ spin–orbit peaks in the Fe 2p XPS spectra, respectively. The result suggest the Fe species located on the Fe@Mn@CNTs and the Fe@CNTs surface is mainly composed of trivalent Fe_2O_3.[36] The Fe $2p_{3/2}$ peak is fitted into three peaks centered at 709.8, 711.1, and 712.8 eV, which related to the Fe^{3+} ion in the Fe_2O_3 structure and the Fe^{3+} bonded with hydroxyl groups.[24] Considering the abundant functional groups located on the CNTs surface, the ratio of the Fe^{3+}-hydroxyl groups could reflect the interaction among Fe species, Mn species and CNTs supports. As listed in Table1, the Fe^{3+}-hydroxyl groups in the Fe@Mn@CNTs is 29.9% and the ratio has decreased to 19.8% for the Fe@CNTs, illustrating the strong synergistic effect in the multi-shelled structure. Additionally, the surface hydroxyl groups are related to the weak acid sites on the catalyst surface. Thus, it can be predicted that the amounts of weak acid sites on the Fe@Mn@CNTs should be larger than that of the Fe@CNTs. It is generally recognized that the Fe^{3+} species (Fe^{3+} and Fe^{3+}-hydroxyl groups) have higher catalytic activities than the Fe^{2+} species over the Fe-based catalysts. [28] Thus, the trivalent Fe_2O_3 on the catalyst surface should also be a crucial component that participates in the NH_3-SCR reaction.

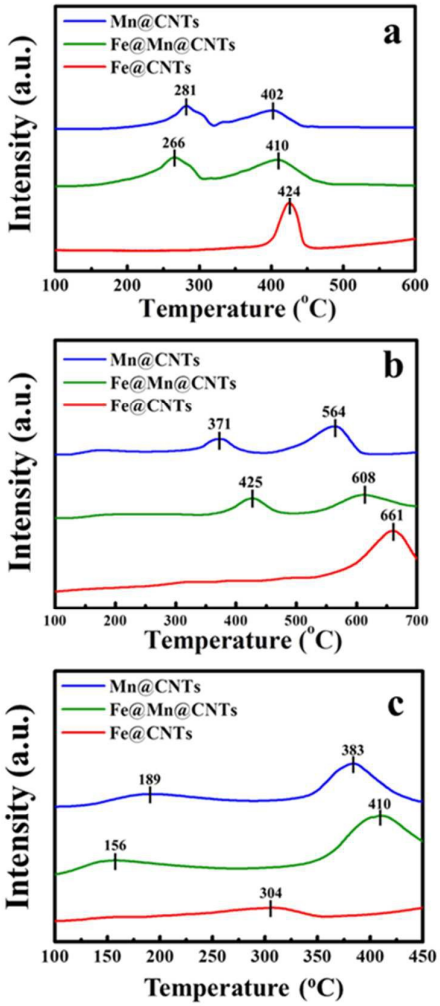

Fig.6 a) H_2-TPR, b) NH_3-TPD and c) $NO+O_2$-TPD profiles of the catalysts.

Journal Name

ARTICLE

Table 1 XPS results of the catalysts

sample	Surface composition (at.%)			O_α/O (%)	Mn^{2+}/Mn (%)	Mn^{3+}/Mn (%)	Mn^{4+}/Mn (%)	Fe^{3+}-OH/Fe (%)
	O	Mn	Fe					
Mn@CNTs	30.0	7.57	–	60.1	17.6	40.6	41.8	–
Fe@Mn@CNTs	32.4	3.71	5.30	66.2	23.8	46.7	29.5	29.9
Fe@CNTs	33.0	0.03	7.30	56.6	–	–	–	19.8

The H_2-TPR was used to investigate the reducibility of the surface reducible species of the two catalysts (Fig.6a). In the H_2-TPR profile of Mn@CNTs, two distinct reduction peaks located at 282 and 402 °C, which correspond to the two step-wise reductions of $MnO_2 \rightarrow Mn_2O_3$ and $Mn_2O_3 \rightarrow MnO$.[15] Since the MnO could not reduce to metallic Mn below 600 °C, no additional peaks occurred in the reduction profile of Mn@CNTs. In the case of Fe@Mn@CNTs, two stronger reduction peaks can also be observed in the H_2-TPR curve. The first peak centered at 265 °C stands for the reduction of MnO_2 and the lower reduction temperature indicates the MnO_2 species become more reducible. As is well known, the crystalline degree could directly affect the reduction ability of the surface species. Thus, the H_2-TPR results point out the surface MnO_2 species turn into more amorphous form after the galvanic replacement reaction, which is consistent with the XRD analysis. It is worth noticing that the second reduction peak become broader and slightly shifted to higher temperature region. According to the study by Putluru et al., the peak could be assigned to the conjunction of the two reduction reactions as $Mn_2O_3 \rightarrow MnO$ and $Fe_2O_3 \rightarrow Fe$,[16] which could reveal the strong interaction between the manganese and the iron species. Different from the Mn containing catalysts, only one peak located at 424 °C occurred in the TPR profile of Fe@CNTs. Based on the XRD and XPS results, the manganese oxide species were proved to be replaced by ferric oxide species. Therefore, the single peak should be attributed to the reduction from Fe^{3+} to the metallic Fe^0. The area of the reduction peak is directly related to the consumption of H_2 and can reflect the amount of reducible species. Combined with the XRD and HR-TEM observing, more reducible species existed in the Fe@Mn@CNTs, which originate from the amorphous structure from the galvanic displacement. The increased reducible species could lead to increased reducibility of the catalysts, thereafter enrich the NH_3-SCR catalytic cycle.

As is well known, the NH_3 molecule can be absorbed on the acid sites and serve as intermediates for the NH_3-SCR of NO. Therefore, The NH_3-TPD analyses were performed to estimate and characterize the distribution of acid sites on the catalysts surface. As shown in Fig.6b, the Mn@CNTs catalyst demonstrated three desorption peaks at 182, 371 and 564 °C, while the Fe@Mn@CNTs catalyst showed stronger and boarder peaks centered at 243, 425 and 608 °C. Besides, the signal of the NH_3 desorption only occurred at 661 °C for the Fe@CNTs. According to the literatures, the desorption peaks in the NH_3-TPD curves correspond to the NH_3 bound to the acid sites on the catalysts surface, while the position of desorption peak is reflecting the strength of the acid sites of catalysts, and the peak area stands for the adsorption amount of NH_3.[43-45] Thus, it is obvious that the amount of acid sites and the strength of those acid sites have been enhanced after the forming of the Fe@Mn@CNTs multi-shell structure, which is beneficial for the catalytic activity.

The formation of surface NO_x species is a crucial step during the NH_3-SCR reaction. To characterize the adsorptive status of the catalyst surface $NO+O_2$-TPD was conducted (Fig.6c).The Fe@Mn@CNTs exhibits two distinct desorption peaks located at 156 and 410 °C. For Mn@CNTs, two obvious peaks at 189 and 383 °C were observed. In the TPD profiles of Fe@CNTs, only one small peak could be found at 304 °C. The low temperature peak (below 200 °C) can be ascribed to the decomposing of surface nitrites, while the peak at high temperature (over 200 °C) can be assigned to bridged and bidentate nitrates decomposition.[46,47] According to the work presented by Huang et.al, the decomposition of the surface nitrites mainly leads to the desorption of NO, while the decomposition of the bridged and bidentate nitrates can cause the desorption of both NO and NO_2 species. [48] Thus, both of the surface NO_x compounds are active in the SCR reaction, especially for the surface nitrites. By comparing the desorption profiles of the catalysts, it is clear that the area of the desorption peaks of Fe@Mn@CNTs are larger than those of Mn@CNTs and Fe@CNTs, indicating the adsorption capability has been greatly enhanced by the formation of the multi-component structure. In summary, the *in-situ* coating of Fe_2O_3 shell could effectively enhance the adsorption of reactants, which is crucial for the de-NO_x process.

Improvement of catalytic activity

Fig.7a depicts the NH_3-SCR activity of the catalysts within the

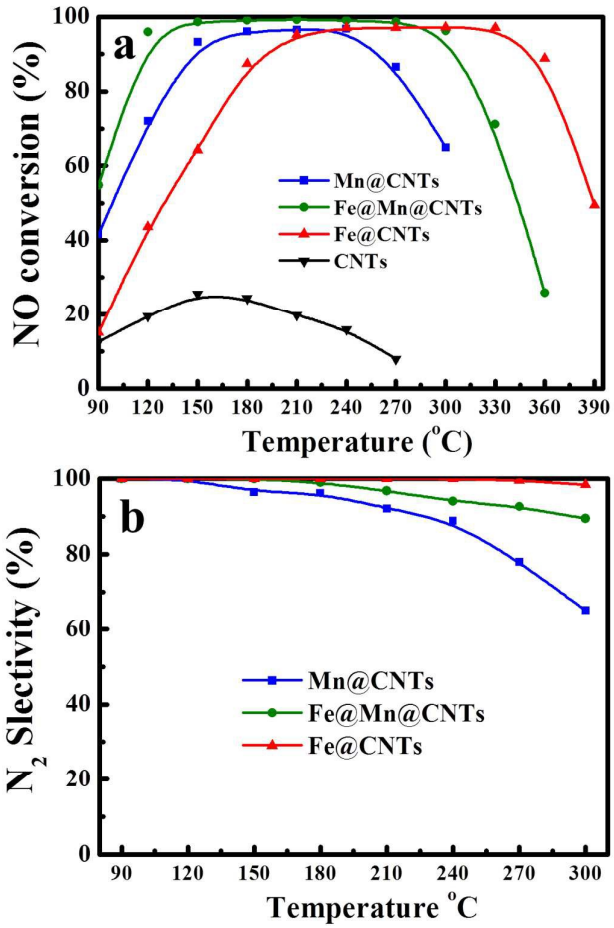

Fig.7 NH_3-SCR performance of the catalysts, a) Catalytic activity and b) N_2 selectivity *Reaction conditions*: [NH_3] = [NO] = 550 ppm, [O_2] = 5 vol. %, N_2 as balance gas, GHSV=20000 h^{-1}.

temperature from 90-390 °C. The pure CNTs catalysts exhibits poor de-NO_x activity among the testing period, while the NO conversion mainly originats from the adsorption-desorption of NO.[19] The Mn@CNTs catalyst demonstrated a well-defined catalytic performance ranging from 150-270 °C and the maximum NO conversion rate of 94% was reached at 210 °C. However, the NO conversion of Mn@CNTs catalyst sharply decreased when the reaction temperature was beyond 270 °C. To reveal the role of the Fe_2O_3 in the SCR reaction, the Fe@CNTs was also tested in the same reaction condition. As depicted in Fig.7a, the catalytic activity raised with the temperature and de-NO_x activity reached 90 % at 210 °C, while the good catalytic activity kept constant until the temperature reached 360 °C. Compared with the manganese oxides, the ferric oxides present a better de-NO_x performance at higher temperature. It is remarkable to note that the Fe@Mn@CNTs demonstrated a wider operation temperature window than that of Mn@CNTs, both in the low temperature and high temperature region. From the XPS results, we observe the declination of Mn^{4+} on the catalysts surface after the galvanic displacement, which may result in the loss of low temperature catalytic activity of Fe@Mn@CNTs catalyst. Nonetheless, many beneficial effects were induced with the formation of the multi-shell structure. From the EDS-mapping and the XPS analyses, we confirmed that the Fe^{3+} species were introduced by galvanic replacement reaction and located at the surface of the Fe@Mn@CNTs catalyst. As well documented in literature, the Fe^{3+} species should also be a crucial component that participates in the NH_3-SCR reaction.[28] Moreover, the amorphous characteristic of the Fe@Mn@CNTs catalyst lead to enhancement of the reducibility as well as the reducible species, which could enrich the NH_3-SCR catalytic cycle. Meanwhile, the increased O_α species on the catalyst surface could facilitate the "Fast SCR" process and promote the catalytic reduction of NO in the low temperature range. Additionally, the adsorption behavior for the reagents has been greatly enhanced by the coating of Fe, which is crucial for the activation of the NH_3 and NO. Those factors lead to an increase to the low temperature de-NO_x activity of the Fe@Mn@CNTs catalysts. On the other hand, the dramatic decrease of the N_2 selectivity of the Mn@CNTs can be observed above 240 °C (Fig.7b), indicating the deactivation of the Mn@CNTs originated from the non-selective oxidation of NH_3. In contrast, the Fe species have proved to be an excellent de-NO_x component with high N_2 selectivity. Thus, the uniformly decoration of the Fe_2O_3 on the outer surface could effectively improve the N_2 selectivity and the Fe@Mn@CNTs catalyst kept over 80% N_2 selectivity at 300 °C, which could explain the good catalytic performance at higher working temperature. The Fe@Mn@CNTs catalyst also demonstrate relatively higher catalytic activity than the Fe-Mn/CNTs IM (prepared by impregnation method and through high temperature calcination, Fig.S2, ESI), confirming the advantages of the well-ordered structure and our design route. Additionally, the stability of the Fe@Mn@CNTs and Mn@CNTs catalysts were tested at 210 °C for 60 hours (Fig.S3a, ESI). The de-NO_x performance of the Mn@CNTs started to slightly decrease after 23 hours, and the catalytic activity decreased to 89% within 60 hour testing time. Conversely, the Fe@Mn@CNTs retained the high NO conversion of 96% during the stability test. The catalysts through stability test were examined by the XRD measurement and the characteristic peak of NH_4NO_3 occurred in the XRD pattern of Mn@CNTs (Fig.S4, ESI), illustrating the decrease of the catalytic activity is derived from the blocking effect of the NH_3NO_3. Fortunately, the NH_4NO_3 diffraction is absent for the Fe@Mn@CNTs and that could explain the excellent stability of the catalyst. Moreover, the Fe@Mn@CNTs catalyst has been tested under lower NO conversion rate for 60 h (Fig.S3b, ESI) to prevent the unobservable deactivation of the catalyst at 100% conversion and the catalyst still presents stable NO conversion under the 60 h duration. Besides, the Fe@Mn@CNTs also demonstrated desirable anti-H_2O performance (Fig.S5, ESI). Generally, the Fe@Mn@CNTs catalyst demonstrates excellent catalytic stability and H_2O resistance, which reveals the strong thermal and structural stability of the multi-shelled catalyst.

Improvement of SO_2 tolerance

As is well known, the effluent gases from stationary sources always contains trace amount of SO_2, which could have negative effects on the de-NO_x catalysts. Thus, the SO_2 deactivation experiments were carried out to clarify the impacts of SO_2 on the Mn@CNTs and Fe@Mn@CNTs. Fig.8a

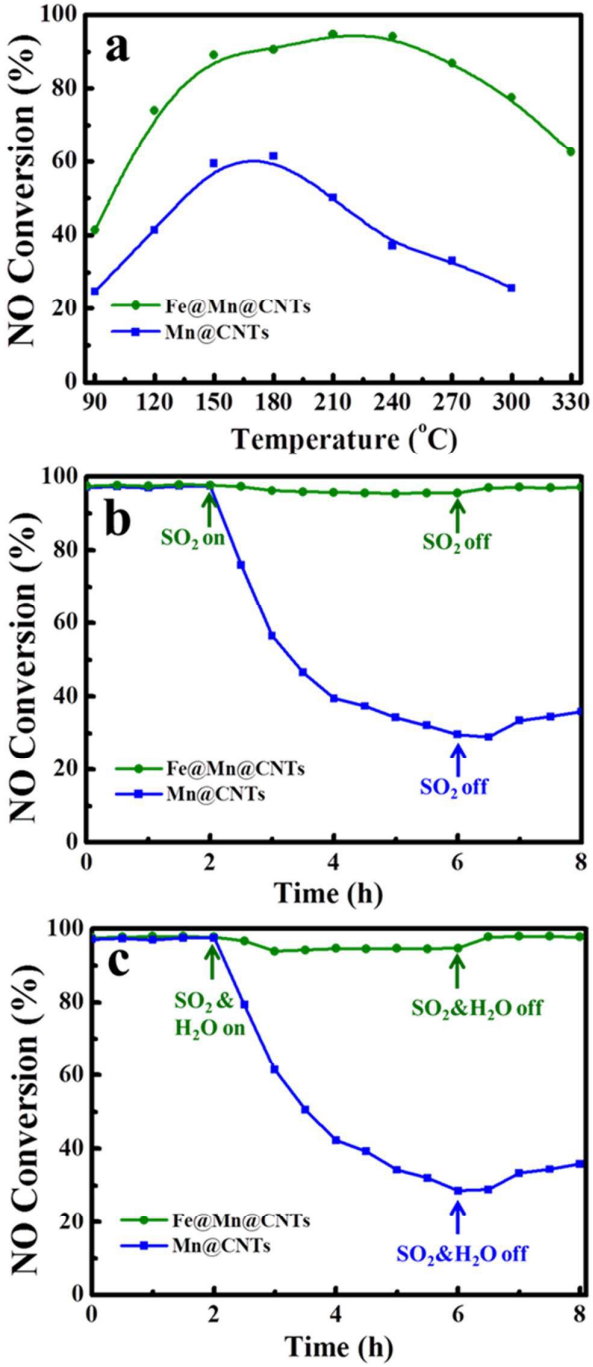

Fig.8 SO_2 resistance of the catalysts, a) Catalytic activity with SO_2, b) SO_2 tolerance test and c) SO_2 & H_2O tolerance test. *Reaction conditions:* $[NH_3] = [NO] = 550$ ppm, $[O_2] = 5$ vol. %, $[SO_2] = 100$ ppm, $[H_2O] = 10$ vol. % (when used), N_2 as balance gas, GHSV=20000 h^{-1}.

illustrates the effect of SO_2 on the SCR activity over the two catalysts as a function of temperature. Obviously, with the presence of 100 ppm SO_2, the catalytic activity of Mn@CNTs was severely suppressed and the maximum NO conversion of 58% could only be reached at 180 °C. Inspiringly, the catalytic activity of Fe@Mn@CNTs is barely affected by the SO_2 in the feed gas, and exhibits an over 85% NO conversion temperature window from 150 to 270 °C (Fig.8b). To further evaluate their SO_2 duration performance, the two catalysts were tested at a typical temperature of 240 °C for 8 hours. As shown in Fig.8b, with the absence of SO_2, the two catalysts kept a high NO conversion at 97% and 95%, respectively. When 100 ppm of SO_2 was added into the inlet gas, only slight inhibition effect of SO_2 can be observed in the case of Fe@Mn@CNTs and the NO conversion over the catalyst maintained at ca. 94%. In contrast, the deNO_x activity of Mn@CNTs dropped continuously within the test period and decreased to 26 % after 4 hours. After the removal of the SO_2 gas, the catalytic activity of Fe@Mn@CNTs catalyst restored to 95%, while the de-NO_x activity of Mn@CNTs only returned to 36%, far from the initial level. Moreover, with the co-existence of the SO_2 and H_2O (Fig.8c), the catalytic activity of the Fe@Mn@CNTs only dropped to 91%, as compared with the sharp declination of the NO conversion of Mn@CNTs.

In order to achieve deeper insights of the sulfur resistance of the Fe@Mn@CNTs catalyst, we investigated the surface composition of the two catalysts through the anti-toxic test by XRD and TGA analyses. Compared to the XRD pattern of the fresh catalysts (Fig.2) and the base line, several additional peaks occurred in the XRD pattern of the two spent catalysts (Fig. 9a). The peak located around 30° could be assigned to the manganese sulfate (JPCDS 74-0877) and the other peaks were too weak for identification. For Mn@CNTs, the stronger characteristic peak of the manganese sulfate species could be observed, reflecting the severe sulfation of the MnO_2 species. In contrast, the over-coated of Fe_2O_3 could serve as a protective layer to restrain the formation of manganese sulfate, which could reduce the deactivation effect of SO_2. Moreover, Qu et al. revealed the sulfation of ferric oxides on the CNTs could intensify the surface acidity as well as the NH_3 adsorption ability of the catalyst, then active the catalysts surface and promote the SCR activity.[25] A similar promotional mechanism can also be found in the catalysts system of V_2O_5/CNTs and CeO_2/TiO_2.[49-51] Considering the high content of Fe species were located on the outer surface of Fe@Mn@CNTs determined by XPS, the high sulfur resistance should be offered by the fine design of the multi-shell structure, especially for the transformation from the surface manganese oxide species to the Fe_2O_3. Additionally, the peak related to ammonia sulfate is absent in the XRD pattern of the spent catalysts. It is well documented that the ammonia sulfate could start to decompose over 200 °C, [52]and the CNTs support can decrease the decomposition temperature of ammonia sulfate.[49] Therefore, it is reasonable to deduce that the decomposition of the ammonia sulfate is the main factor for the restoration of catalytic activity after eliminating the SO_2 gas. The TGA test (Fig.9b) was performed to investigate the amount of the sulfate species on the catalysts surface. The initial weight loss is related to the adsorbed water and the surface hydroxyl groups,[53] while the decomposition of surface sulfate species lead to the weight loss ranging from 300-500 °C.[12] When the testing temperature reached to 500 °C, the CNTs started to decompose and caused the dramatic decrease of the weight of the catalysts.[54] As shown clearly, the weight loss of Fe@Mn@CNTs catalyst (3.4%) catalyst is much lower than that of Mn@CNTs (6.5%) in the temperature range of

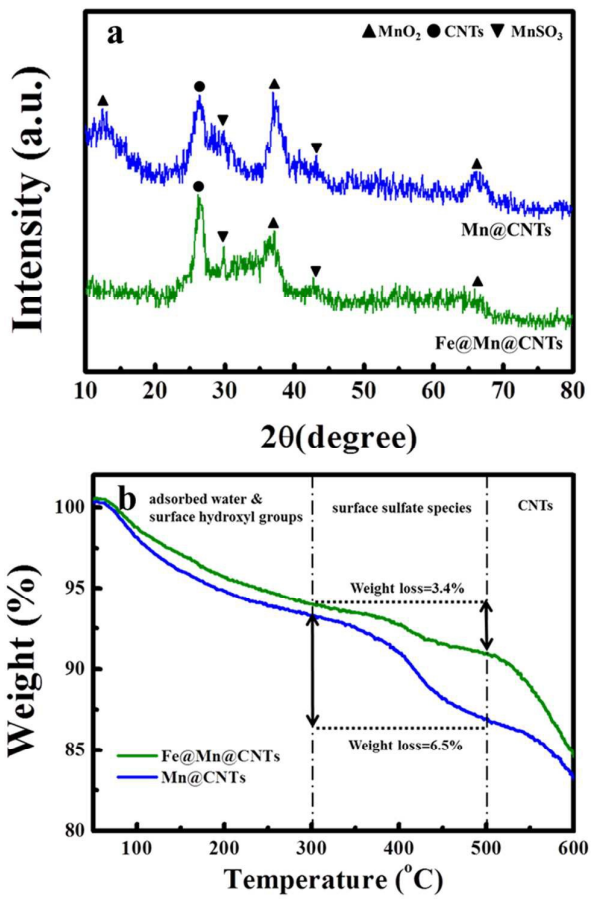

Fig.9 a) XRD patterns and b) TGA curves of the catalysts after the SO_2 tolerance test.

300-500 °C. The result indicates less sulfate species was formed on the surface of Fe@Mn@CNTs catalyst, which provides strong evidence for the anti-sulfation ability of the Fe_2O_3 shell.

The states of the SO_2 on the catalysts surface were investigated by SO_2+O_2 TPD and the profiles are shown in Fig.10. For both catalysts, the SO_2 release peaks can be observed at the temperature range around 300 °C and 500 °C, which corresponded to the weakly adsorbed or the physisorbed SO_2 and the decomposition of the surface metal sulfates.[55,56] Obviously, the SO_2 adsorption amount at high temperature range over Mn@CNTs catalyst is significantly higher than that of Fe@Mn@CNTs catalyst. It indicates more metal sulfates should be generated without the protection of the Fe_2O_3 shell, which agrees well with the XRD and TGA tests. As is well documented in the literature, the deactivation of the catalysts could originate from the sulfating of the surface metal oxides (which is irreversible) and the deposition of ammonia sulfate on the surface active sites (which can be vanished).[57-60] Therefore, it is clear that the accumulation of sulfated Mn species could be the main reason for the deactivation of Mn@CNTs. Meanwhile, the formation of the Fe_2O_3 shell could promote the alkalinity on the catalyst surface, thereafter suppressed the formation of sulfate species. That could be an important factor explaining the high SO_2 tolerance of Fe@Mn@CNTs catalyst.

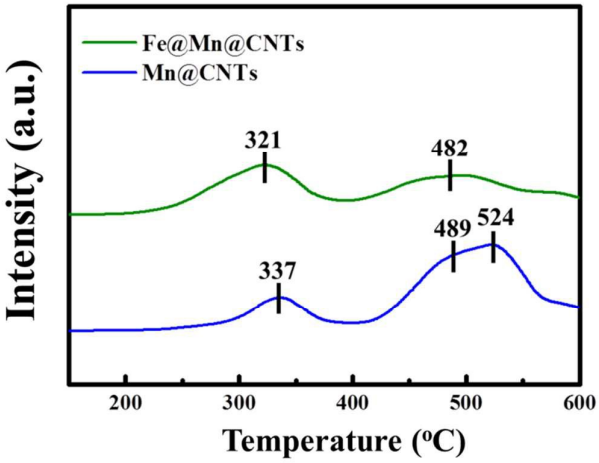

Fig.10 SO_2+O_2-TPD profiles of the catalysts.

4. Conclusions

In this work, we successfully developed the multi-layered Fe_2O_3@MnO_x@CNTs catalyst *via* a facile and green synthesis pathway. Inspiringly, the multi-shell catalyst demonstrates outstanding low temperature catalytic performance, improved N_2 selectivity as well as impressive anti-sulfur ability, which meet well with our expectations. Exploiting the systematical investigation, we reveal the galvanic reaction can not only lead to the formation of the multi-shell structure, but also enhance the surface reducible species, the O_α species as well as the surface adsorption behavior. Moreover, the over-coated Fe_2O_3 could restrain the formation of surface sulfate species, which could result in the high SO_2 tolerance of the catalyst. Those favorable properties imply that the synthetic protocol could be a common way to overcome the drawbacks of the Mn based SCR catalysts.

Acknowledgements

The authors acknowledge the support of the National Basic Research Program of China (973 Program, 2014CB660803), the National Natural Science Foundation of China (U1462110), the Science and Technology Commission of Shanghai Municipality (13NM1401200), and the Shanghai Municipal Education Commission (14ZZ097).

References

1. Z. Huang, X. Gu, W. Wen, P. Hu, M. Makkee, H. Lin, F. Kapteijn and X. Tang, *Angew. Chem.*, 2013, **52**, 660-664.
2. W. Wang, G. McCool, N. Kapur, G. Yuan, B. Shan, M. Nguyen, U. M. Graham, B. H. Davis, G. Jacobs, K. Cho and X. Hao, Science, 2012, **337**, 832-835.
3. S. Beirle, K. F. Boersma, U. Platt, G. Lawrence and T. Wagner, *Science*, 2011, **333**, 1737-1739.
4. C. Paolucci, A. A. Verma, S. A. Bates, V. F. Kispersky, J. T. Miller, R. Gounder, W. N. Delgass, F. H. Ribeiro and W. F. Schneider, *Angew. Chem.*, 2014, **53**, 11828-11833.
5. Z. Liu, S. Zhang, J. Li, J. Zhu and L. Ma, *Appl. Catal., B*, 2014, **158-159**, 11-19.

6. K. Lee, P. Kumar, M. Maqbool, K. Rao, K. Song and H. Ha, *Appl. Catal., B*, 2013, **142-143**, 705-717.
7. A. Kompio, A. Brückner, F. Hipler, G. Auer, E. Löffler and W. Grünert, *J. Catal.*, 2012, **286**, 237-247.
8. R. Gao, D. Zhang, X. Liu, L. Shi, P. Maitarad, H. Li, J. Zhang and W. Cao, *Catal. Sci. Technol.*, 2013, **3**, 191-199.
9. M. M. Shafer, B. M. Toner, J. T. Overdier, J. J. Schauer, S. C. Fakra, S. Hu, J. D. Herner and A. Ayala, *Environ. Sci. Technol.*, 2012, **46**, 189-195.
10. R. Ettireddy, N. Ettireddy, S. Mamedov, P. Boolchand and P. G. Smirniotis, *Appl. Catal., B*, 2007, **76**, 123-134.
11. S. Cai, D. Zhang, L. Shi, J. Xu, L. Zhang, L. Huang, H. Li and J. Zhang, *Nanoscale*, 2014, **6**, 7346-7353.
12. H. Chang, X. Chen, J. Li, L. Ma, C. Wang, C. Liu, J. W. Schwank and J. Hao, *Environ. Sci. Technol.*, 2013, **47**, 5294-5301.
13. X. Wang, Y. Zheng, Z. Xu, X. Wang and X. Chen, *RSC Adv.*, 2013, **3**, 11539.
14. R. Ettireddy, N. Ettireddy, T. Boningari, R. Pardemann and P. G. Smirniotis, *J. Catal.*, 2012, **292**, 53-63.
15. B. Thirupathi and P. G. Smirniotis, *J. Catal.*, 2012, **288**, 74-83.
16. S. S. R. Putluru, L. Schill, A. D. Jensen, B. Siret, F. Tabaries and R. Fehrmann, *Appl. Catal., B*, 2015, **165**, 628-635.
17. F. Liu, W. Shan, Z. Lian, L. Xie, W. Yang and H. He, *Catal. Sci. Technol.*, 2013, **3**, 2699.
18. X. Fan, F. Qiu, H. Yang, W. Tian, T. Hou and X. Zhang, *Catal. Commun.*, 2011, **12**, 1298-1301.
19. C. Fang, D. Zhang, L. Shi, R. Gao, H. Li, L. Ye and J. Zhang, *Catal. Sci. Technol.*, 2013, **3**, 803-811.
20. Z. Ma, H. Yang, Q. Li, J. Zheng and X. Zhang, *Appl. Catal., A*, 2012, **427-428**, 43-48.
21. C. Fang, D. Zhang, S. Cai, L. Zhang, L. Huang, H. Li, P. Maitarad, L. Shi, R. Gao and J. Zhang, *Nanoscale*, 2013, **5**, 9199-9207.
22. S. Pan, H. Luo, L. Li, Z. Wei and B. Huang, *J. Mol. Catal. A*, 2013, **377**, 154-161.
23. H. Chang, J. Li, X. Chen, L. Ma, S. Yang, J. W. Schwank and J. Hao, *Catal. Commun.*, 2012, **27**, 54-57.
24. J. Han, D. Zhang, P. Maitarad, L. Shi, S. Cai, H. Li, L. Huang and J. Zhang, *Catal. Sci. Technol.*, 2015, **5**, 438-446.
25. L. M. Zhen, P. Wang and Q. Fu, *Chem. Commun.*, 2015, **51**, 956-958.
26. S. Yang, C. Liu, H. Chang, L. Ma, Z. Qu, N. Yan, C. Wang and J. Li, *Ind. Eng. Chem. Res.*, 2013, **52**, 5601-5610.
27. Y. Shu, T. Aikebaier, X. Quan, S. Chen and H. Yu, *Appl. Catal., B*, 2014, **150-151**, 630-635.
28. X. Mou, B. Zhang, Y. Li, L. Yao, X. Wei, D. S. Su and W. Shen, *Angew. Chem.*, 2012, **51**, 2989-2993.
29. S. Yang, J. Li, C. Wang, J. Chen, L. Ma, H. Chang, L. Chen, Y. peng and N. Yan, *Appl. Catal., B*, 2012, **117-118**, 73-80.
30. S. Yang, S. Xiong, Y. Liao, X. Xiao, F. Qi, Y. Peng, Y. Fu, W. Shan and J. Li, *Environ. Sci. Technol.*, 2014, **48**, 10354-10362.
31. X. Wei, Y. Li and W. Shen, *RSC Adv.*, 2015, **5**, 66141-66146.
32. D. Zhang, L. Zhang, L. Y. Shi, C. Fang, H. Li, R. Gao, L. Huang and J. Zhang, *Nanoscale*, 2013, **5**, 1127-1136.
33. M. H. Oh, T. Yu, S. H. Yu, B. Lim, K. T. Ko, M. G. Willinger, D. H. Seo, B. H. Kim, M. G. Cho, J. H. Park, K. Kang, Y. E. Sung, N. Pinna and T. Hyeon, *Science*, 2013, **340**, 964-968.
34. F. Arena, T. Torre, C. Raimondo and A. Parmaliana, *Phys. Chem. Chem. Phys.*, 2001, **3**, 1911-1917.
35. B. D. Anderson and J. B. Tracy, *Nanoscale*, 2014, **6**, 12195-12216.
36. X. Hui, T. Tan, H. Yu, W. Liu, C. Xu, Z. Xu, H. Hng, Q. Yan, *ACS nano*, 2014, **8**, 4004–4014.
37. H. Zhang, H. Wang, N. Zhou, J. Chen, Y. Tang, and J. Huang, *Nanoscale*, 2014, **6**, 10235-10242.
38 K. Yang, and B. Xing, *Environ. Sci. Technol.*, 2006, **40**, 1855.
39. L. Zhang, L. Shi, L. Huang, J. Zhang, R. Gao and D. Zhang, *ACS Catal.*, 2014, **4**, 1753-1763.
40. M. Koebel, G. Madia, F. Raimondi and A. Wokaun, *J. Catal.*, 2002, **209**, 159-165.
41. F. Liu. H. He, *J. Phys. Chem. C*, 2010, **114**, 16929-16936.
42. F. Liu, H. He, Y. Ding and C. Zhang, *Appl. Catal., B*, 2009, **93**, 194-204.
43. S. A. Bates, W. N. Delgass, F. H. Ribeiro, J. T. Miller and R. Gounder, *J. Catal.*, 2014, **312**, 26-36.
44. T. Yu, J. Wang, M. Shen and W. Li, *Catal. Sci. Technol.*, 2013, **3**, 3234.
45. F. Cao, J. Chen, C. Lyu, M. Ni, X. Gao and K. Cen, *Catal. Sci. Technol.*, 2015, **5**, 1267-1279.
46. L. Ma, Y. Cheng, G. Cavataio, R. W. McCabe, L. Fu and J. Li, *Appl. Catal., B*, 2014, **156-157**, 428-437.
47. Z. Lian, F. Liu, H. He, X. Shi, J. Mo and Z. Wu, *Chem. Eng. J.*, 2014, **250**, 390-398.
48. B. Guan, H. Lin, L. Zhu, B. Tian and Z. Huang, *Chem. Eng. J.*, 2012, **181-182**, 307-322.
49. S. Bai, J. Zhao, L. Wang and Z. Zhu, *Catal. Today*, 2010, **158**, 393-400.
50. L. Zhang, L. Li, Y. Cao, X. Yao, C. Ge, F. Gao, Y. Deng, C. Tang and L. Dong, *Appl. Catal., B*, 2015, **165**, 589-598.
51. Q. Li, H. Yang, F. Qiu and X. Zhang, *J. Hazard. Mater.*, 2011, **192**, 915-921.
52. F. Liu and H. He, *Catal. Today*, 2010, **153**, 70-76.
53. J. Huang, Z. Tong, Y. Huang and J. Zhang, *Appl. Catal., B*, 2008, **78**, 309-314.
54. T. Das, S. Banerjee, K. Dasgupta, J. B. Joshic and V. Sudarsana, *RSC Adv.*, 2015, **5**, 41468-41474.
55. C. Liu, L. Chen, J. Li, L. Ma, H. Arandiyan, Y. Du, J. Xu and J. Hao, *Environ. Sci. Technol.*, 2012, **46**, 6182-6189.
56. J. Li, Y. Zhu, R. Ke and J. Hao, *Appl. Catal., B*, 2008, **80**, 202-213.
57. W. Xu, and Y. Yu, *J. Phys. Chem. C*, 2009, **113**, 4426-4432.
58. Y. Wang, X. Li, L. Zhan, C. Li, W. Qiao and L. Ling, *Ind. Eng. Chem. Res.*, 2015, **54**, 2274-2278.
59. Z. Ma, H. Yang, F. Liu and X. Zhang, *Appl. Catal., A*, 2013, **467**, 450-455.
60. Z. Ma, H. Yang, B. Li, F. Liu and X. Zhang, *Ind. Eng. Chem. Res.* 2013, **52**, 3708−3713.